Taylor & Francis
Taylor & Francis Group

HEAT TRANSFER CONDITIONS IN FLOW ACROSS A BUNDLE OF CYLINDRICAL AND ELLIPSOIDAL TUBES

Andrej Horvat and Borut Mavko
"Jožef Stefan" Institute, Reactor Engineering Division, Jamova, Ljubljana, Slovenia

Transient numerical simulations of fluid and heat flow are performed for a number of heat exchanger segments with cylindrical and ellipsoidal form of tubes in a staggered arrangement. Based on the recorded time distributions of velocity and temperature, time-average values of Reynolds number, drag coefficient, and Stanton number are calculated. The drag coefficient and the Stanton number are smaller for the ellipsoidal tubes than for the cylindrical tubes. With an increasing hydraulic diameter, the difference between the two forms of tubes diminishes. To validate the selected numerical approach, the calculated time-average values are compared with experimental data. The time-average values are further used to construct the drag coefficient and the Stanton number as polynomial functions of Reynolds number and hydraulic diameter. The polynomial functions obtained are to be used as input correlations for a heat exchanger integral model.

1. INTRODUCTION

The heat transfer industry, especially the electronic packaging sector, requires precise and fast prediction of drag and heat transfer for different shapes of heat exchanging surfaces. In general, these can be assessed by experimental testing (e.g., [1–4]) and by numerical calculations (e.g., [5–13]). Over the years, a lot of experimental as well as modeling work has been done in the area of heat exchangers. We mention only a few works, as it is impossible to justly evaluate work of all investigators who made important contributions.

Due to the nature of experimental work, which enables researchers to analyze only a few heat exchanger geometries with slightly varied geometry parameters, the experimental investigation of all prototype geometries is not feasible. As an affordable substitute, numerical approaches and methods have been increasingly employed to simulate processes in heat exchangers in order to find new designs for emerging technological needs. Nevertheless, the direct numerical simulation of the heat

NOMENCLATURE

a and b	maximum and minimum radii of the ellipsoidal tubes	t	time	
A_f	fluid flow cross section ($= V_f/2l_x$)	t_{scale}	average time needed for a flow particle to pass the simulation domain	
A_o	wetted surface			
c	speed of sound	T	temperature	
c_p	specific heat	u	streamwise velocity	
C_d	drag coefficient	v	velocity	
$\overline{C}_d$	time-average drag coefficient	V_f	fluid volume in REV	
d	diameter	y^+	nondimensional wall distance	
dt	timestep	ε	turbulence dissipation rate	
d_h	hydraulic diameter ($= 4V_f/A_o$)	μ	dynamic viscosity	
F_1	blending function in the SST model	ρ	density	
h	height of REV	ω	turbulence frequency	
k	turbulence kinetic energy			
l	pitch between tubes			
p	pressure	**Subscripts and Superscripts**		
Pr	Prandtl number	t	turbulence model variable	
Re	Reynolds number	wall	wall conditions	
REV	representative elementary volume	x	streamwise direction	
St	Stanton number	y	horizontal spanwise direction	
$\overline{\text{St}}$	time-average Stanton number	z	vertical spanwise direction	

transfer processes in heat exchangers is still computationally too demanding. Therefore, significant simplifications, especially in the turbulence modeling and the wall effect treatment, are necessary.

Horvat and Mavko [14] used an alternative approach based on hierarchic modeling, which was proposed by Patankar and Spalding [15]. In implementing this approach, the model and its computation are split onto two distinct levels. On the first level, transient three-dimensional numerical simulations of fluid and heat flow in a geometry similar to a heat exchanger segment are performed to study local thermohydraulic behavior. Based on the calculated three-dimensional velocity and temperature distributions, local values of the drag coefficient and of the heat transfer coefficient are determined. On the second level, an integral model [16], which uses the calculated local coefficients as input parameters, is applied to simulate heat transfer processes in a whole heat exchanger. The use of this two-level hierarchic modeling approach has some clear advantages. As these computationally most demanding terms of momentum and heat transport are determined on a separate level, the integral code is fast running, but still capable of accurately predicting the heat flow for a whole heat exchanger.

In this article, we present computational results of fluid and heat flow in heat exchanger segments with cylindrical and ellipsoidal forms of tubes in a staggered arrangement. The numerical simulations cover laminar, transitional, as well as turbulent flow regimes. To adequately model the fluid and heat flow phenomena in the heat exchanger segments, transient numerical simulations with special near-wall treatment were performed. These calculations were used to obtain time-average values of drag coefficient and Stanton number. Based on these values, we constructed drag coefficient $\overline{C}_d$ and Stanton number $\overline{\text{St}}$ as polynomial functions of Reynolds number and a geometric parameter. As the most appropriate geometric parameter, a hydraulic

diameter d_h was chosen. The calculated values of $\overline{C}_d$ and $\overline{St}$ also enabled us to compare aerodynamic and thermal efficiency of cylindrical and ellipsoidal tube bundles.

The constructed polynomial surfaces $\overline{C}_d$ and $\overline{St}$ are probably not a unique solution of the least-squares approximation of the numerical results. Certainly, more numerical results would improve the confidence of the constructed functions. Nevertheless, the obtained polynomial functions $\overline{C}_d$ and $\overline{St}$ represent reliable input data for the heat exchanger integral model [16], which was the main objective of the numerical analysis performed.

2. GEOMETRIC CONSIDERATIONS

The numerical calculations were performed for a representative elementary volume (REV) of a tube bundle with staggered arrangement. It is colored gray in Figure 1. The size and shape of the REV were selected after a fair amount of testing. We took into consideration the error arising from limiting the simulation domain, overall flow dynamics in the simulation domain, and needed computational resources. Based on the tests performed, it was concluded that in order to get representative data, it is more important to simulate longer time intervals than to enlarge the simulation domain.

In the case of the cylindrical tubes the diameter was 3/8 in (9.525 mm). The calculations were performed for four different geometries with different diagonal pitch-to-diameter ratio: $l/d = 1.125$, 1.25, 1.5, and 2.0. For each geometry, the REV height h was equal to the diagonal pitch l. The analysis was limited to bundle arrangements in which the pitch in the x direction, l_x, is equal to the pitch in the y direction, l_y.

The geometries with the ellipsoidal tubes were designed with a ratio 1:1.5 between the maximum and minimum radii (a and b). Furthermore, the size of the tubes was fully defined with the requirement that the fluid volume V_f of the REV has to be equal for the cylindrical and the ellipsoidal tubes:

$$V_{f,\,\text{cyl}} = V_{f,\,\text{ell}}$$
$$h(2l_x l_y - 0.25\pi d^2) = h(2l_x l_y - \pi ab) \qquad (1)$$
$$a = \sqrt{\frac{3}{2}}\frac{d}{2} \quad \text{and} \quad b = \sqrt{\frac{2}{3}}\frac{d}{2}$$
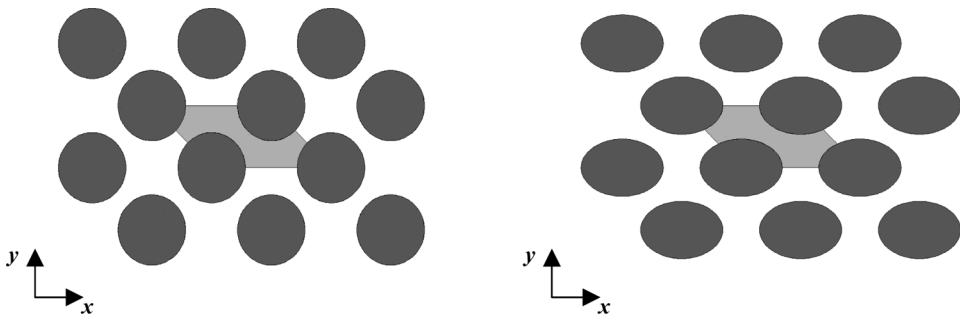
Figure 1. Cross section of heat exchanger structure for $l/d = 1.25$: cylindrical (left) and ellipsoidal (right) forms.

Table 1. Hydraulic diameters d_h for all geometries with cylindrical and ellipsoidal form of tube cross section

l/d	Cylindrical form (cm)	Ellipsoidal form (cm)
1.125	0.5824	0.5649
1.25	0.9424	0.9142
1.5	1.776	1.723
2.0	3.899	3.782

All together, eight different geometric models were built, four for the cylindrical and four for the ellipsoidal form of tube cross sections. Figure 1 presents only two of these geometries, with pitch-to-diameter ratio $l/d = 1.25$. The hydraulic diameter d_h for the each geometry modeled is given in Table 1.

3. MATHEMATICAL MODEL

The commercial code CFX 5.7 was used to perform transient numerical simulations of air flow and heat transfer in the REV. Due to relatively low flow speeds ($v_{max} < 0.1c$), the incompressible flow model was selected. As the basic transport equations (mass, momentum, and thermal energy) in the CFX code can be found in any classical fluid dynamics book (e.g., [17]), they are not repeated here.

The tube walls in the REV were treated as isothermal, with the temperature $T_{wall} = 35°C$. To allow disturbances to propagate over the geometric limits of the simulation domain, periodic boundary conditions were assigned in all three directions for all other boundaries.

In order to model the flow consistently, periodicity had to be imposed on the transport equations in the streamwise direction. In the momentum transport equation, periodicity was achieved by separating an average pressure drop Δp across the simulation domain from its residual part:

$$p = p^* - x\left(\frac{\Delta p}{2l_x}\right) \tag{2}$$

Thus, the momentum transport equation yields

$$\partial_t(\rho v_i) + \partial_j v_j(\rho v_i) = -\partial_j p^* \delta_{ij} + \partial_j(\mu \partial_j v_i) + \left(\frac{\Delta p}{2l_x}\right)\delta_{i,x} + \partial_j(\mu_t \partial_j v_i) - \frac{2}{3}\rho k \delta_{ij} \tag{3}$$

The preset values of pressure drop Δp across the simulation domain were the same for the cylindrical and ellipsoidal forms of tube cross section. They are summarized in Table 2.

Periodicity of the temperature field was introduced by subtracting an average temperature increase ΔT along the simulation domain:

$$T = T^* + x\left(\frac{\Delta T}{2l_x}\right) \tag{4}$$

Table 2. Imposed pressure drop Δp [Pa] over the simulation domain

l/d	1	2	3	4	5	6	7	8
1.125	2.5	5.0	10.0	20.0	40.0	80.0	160.0	—
1.25	0.5	1.0	2.0	4.0	8.0	16.0	24.0	32.0
1.5	0.125	0.25	0.5	1.0	2.0	4.0	6.0	8.0
2.0	0.015625	0.03125	0.0625	0.125	0.25	0.5	0.75	1.0

The energy transport equation changes its form to

$$\partial_t(\rho c_p T^*) + \partial_j v_j(\rho c_p T^*) = \partial_j(\lambda \partial_j T^*) - \rho_f c_p v_j\left(\frac{\Delta T}{2l_x}\right)\delta_{x,j} + \partial_j\left(\frac{\mu_t}{Pr_t}\partial_j c_p T^*\right) \qquad (5)$$

Consequently, the isothermal boundary conditions are converted to

$$T^*_{\text{wall}} = T_{\text{wall}} - x\left(\frac{\Delta T}{2l_x}\right) \qquad (6)$$

In order to preserve validity of the assumption of constant material properties, the average temperature increase was set to $\Delta T = 1°C$ for all simulations.

The turbulence stresses and the turbulence viscosity μ_t were calculated with the transient shear stress transport (SST) model, which was developed and improved by Menter [18]. It is a combination of the $k-\varepsilon$ and the $k-\omega$ models of Wilcox [19]. At the wall, turbulence frequency ω is much more precisely defined than turbulence dissipation rate ε. Therefore, the SST model activates the Wilcox model in the near-wall region by setting the blending function F_1 to 1.0. Far away from the wall, F_1 is 0.0, thus activating the $k-\varepsilon$ model for the rest of the flow field:

$$\text{SST model} = F_1 \cdot (k-\omega \text{ model}) + (1 - F_1) \cdot (k-\varepsilon \text{ model}) \qquad (7)$$

By switching between the two models, the SST model gives similar, if not even superior performance than the low-Reynolds-number $k-\varepsilon$ models, but with much greater robustness. More details on the SST model can be found in [20].

4. SIMULATION DETAILS

Three-dimensional numerical meshes were generated to perform the analysis. They consisted of tetrahedrals and prisms, which were aligned with walls to better approximate the boundary-layer structure. As numerical results can be grid dependent, special care was taken to construct numerical grids with sufficient resolution and uniformity. A basic criterion was the maximum nondimensional wall distance y^+ of the first layer of grid nodes. During the simulations, the maximum y^+ did not exceed 2.0. The number of grid nodes used in each numerical simulation is given in the Appendix.

In order to reduce the computational time required to reach thermal equilibrium, steady-state simulations on a coarser numerical mesh were performed first. After thermal equilibrium was reached, the result files were used as initial conditions for further transient numerical simulations. The time step for the transient calculations was based on an average time interval needed for a flow particle to pass the simulation domain:

$$t_{\text{scale}} = \frac{2l_x}{u_f} \qquad \text{and} \qquad dt = \frac{t_{\text{scale}}}{80} \tag{8}$$

5. RESULTS

Numerical simulations of fluid and heat flow in the REV were performed for cylindrical and ellipsoidal tubes in the staggered arrangement (Figure 1) with four different pitch-to-diameter ratios. The imposed pressure drops Δp (Table 2) across the REV generated the transient flow, which was in most cases unsteady. In order to extract relevant statistical values of physical variables, the volumetric average velocity,

$$u_f(t) = \frac{1}{V_f} \int_{V_f} u(t, x_i) dV \tag{9}$$

and temperature,

$$T_f(t) = \frac{1}{u_f(t)V_f} \int_{V_f} u(t, x_i) T(t, x_i) dV \tag{10}$$

were recorded at each time step after statistical steady-state flow conditions were reached. The length of the recording interval was decided on a case-to-case basis. We tried to find a repeatable pattern of flow behavior. Therefore, the recording intervals were from 1,200 to 4,750 time steps long. This means that the recording interval was at least 150 times longer than the time required for an average flow particle to travel the length of the simulation domain (8).

Using the obtained velocity distributions $u_f(t)$ and the temperature distributions $T_f(t)$, the Reynolds number,

$$\text{Re}(t) = \frac{\rho u_f(t) d_h}{\mu} \tag{11}$$

the drag coefficient,

$$C_d(t) = \frac{2\Delta p}{\rho u_f^2(t)} \left(\frac{A_f}{A_0} \right) \tag{12}$$

and the Stanton number,

$$\text{St}(t) = \frac{\Delta T}{T_{\text{wall}} - T_f(t)} \left(\frac{A_f}{A_0} \right) \tag{13}$$

time distributions were calculated for the each case. Further on, their time averages $\overline{\text{Re}}$, $\overline{C}_d$, and $\overline{\text{St}}$ and their standard deviations S_{Re}, S_{Cd}, and S_{St} were determined.
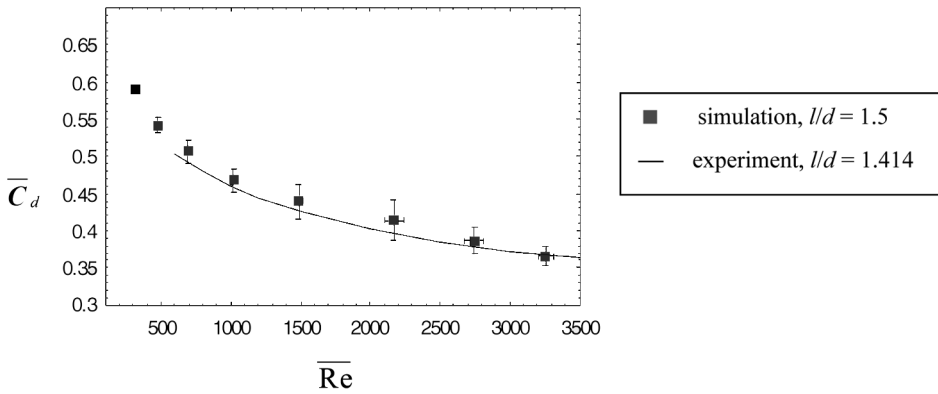
Figure 2. Comparison of the calculated average drag coefficient $\overline{C}_d$ with the experimental data [2]; cylindrical form.

5.1. Validation

To validate the presented numerical approach, the results obtained for one of the cases were compared with the experimental data of Kays and London [2]. For the comparison, we selected the geometry with the cylindrical form of tube cross section and $l/d = 1.5$. The calculated values of drag coefficient $\overline{C}_d$ and Stanton number $\overline{St}$ were compared with the experimental values for a similar geometry with $l/d = 1.414$ (Figures 2 and 3).

The comparison in Figures 2 and 3 shows good agreement between the calculated and the experimentally obtained values of average drag coefficient $\overline{C}_d$ and average Stanton number $\overline{St}$ for the whole range of Reynolds numbers $\overline{Re}$. The agreement demonstrates the correctness of the selected numerical approach. It has also given us confidence to use the same methodology for other cases.
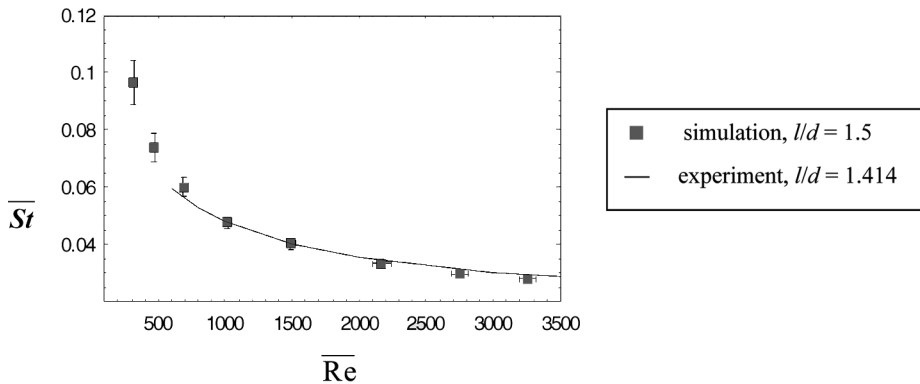
Figure 3. Comparison of the calculated average Stanton number $\overline{St}$ with the experimental data [2]; cylindrical form.

Table 3. Reynolds number $\overline{Re}$ and drag coefficient $\overline{C_d}$ for the cylindrical form

l/d		1	2	3	4	5	6	7	8
1.125	$\overline{Re}$	258	385	549	816	1,178	1,733	2,557	—
	$\overline{C_d}$	0.858	0.773	0.758	0.685	0.658	0.608	0.560	—
1.25	$\overline{Re}$	266	397	590	865	1,248	1,870	2,328	2,841
	$\overline{C_d}$	0.616	0.554	0.501	0.467	0.448	0.400	0.386	0.3465
1.5	$\overline{Re}$	321	473	692	1,019	1,489	2,169	2,746	3,258
	$\overline{C_d}$	0.590	0.542	0.507	0.468	0.439	0.414	0.387	0.366
2.0	$\overline{Re}$	274	443	655	935	1,373	2,029	2,497	2,909
	$\overline{C_d}$	0.801	0.613	0.561	0.551	0.510	0.468	0.463	0.455

5.2. Drag Coefficient Functions

The time distributions of Reynolds number $Re(t)$ and drag coefficient $C_d(t)$ were obtained for both forms of tube cross section and for all the imposed pressure drops (Table 2). The collected statistical averages $\overline{Re}$ and $\overline{C_d}$ are given in Table 3 for the cylindrical form and in Table 4 for the ellipsoidal form of tube cross section.

By using the least-squares approximation, the calculated values in Tables 3 and 4 enabled us to construct $\overline{C_d}$ for each form of tube cross section as a polynomial function of Reynolds number $\overline{Re}$ and hydraulic diameter d_h. For the cylindrical form, the function

$$\overline{C_d}(d_h, \overline{Re}) = 0.2353 + 3.222 \cdot 10^{-10} d_h^{-4} + 1.348 d_h^{1/2}$$
$$+ 64.47 \, \overline{Re}^{-1} - 1.855 \cdot 10^{-5} \, \overline{Re} - 2.118 \cdot 10^{-9} \, \overline{Re}^2 \qquad (14)$$

was obtained. For the ellipsoidal form, we calculated the following function:

$$\overline{C_d}(d_h, \overline{Re}) = 0.03050 + 5.724 \cdot 10^{-4} d_h^{-1} + 0.8838 d_h^{1/2} + 64.30 \, \overline{Re}^{-1}$$
$$- 5.826 \cdot 10^{-4} \, \overline{Re}^{1/2} \qquad (15)$$

Figures 4 and 5 present contour plots of the drag coefficient polynomials for the cylindrical (14) and for the ellipsoidal (15) form of tube cross section.

Table 4. Reynolds number $\overline{Re}$ and drag coefficient $\overline{C_d}$ for the ellipsoidal form

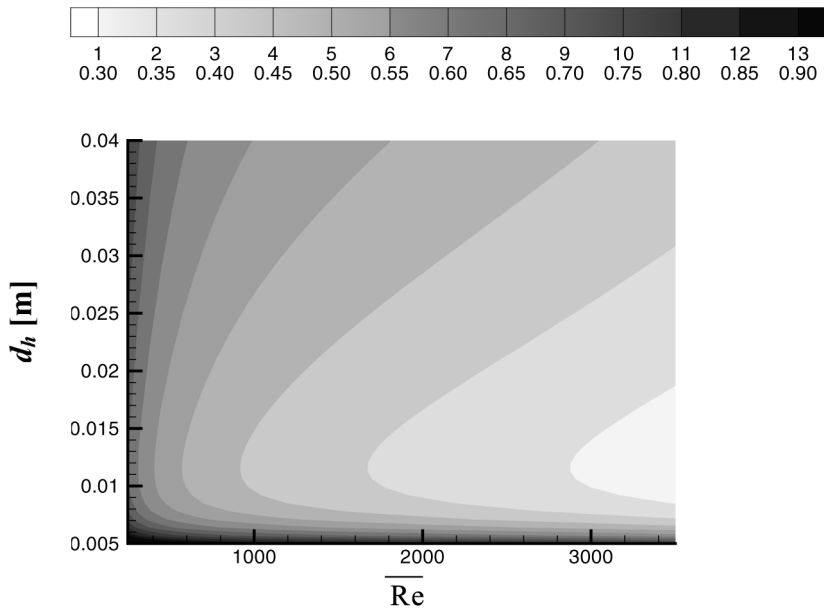| l/d		1	2	3	4	5	6	7	8
1.125	$\overline{Re}$	403	604	871	1,233	1,963	3,081	4,543	—
	$\overline{C_d}$	0.321	0.285	0.275	0.276	0.218	0.176	0.162	—
1.25	$\overline{Re}$	351	513	783	1,167	1,743	2,550	3,179	3,753
	$\overline{C_d}$	0.322	0.302	0.259	0.234	0.209	0.196	0.189	0.180
1.5	$\overline{Re}$	422	670	1,025	1,553	2,312	3,396	4,255	4,957
	$\overline{C_d}$	0.311	0.247	0.211	0.184	0.166	0.154	0.147	0.144
2.0	$\overline{Re}$	351	590	934	1,381	1,999	2,915	3,626	4,234
	$\overline{C_d}$	0.445	0.316	0.252	0.230	0.220	0.207	0.200	0.196

Figure 4. Drag coefficient approximation function (14) for the cylindrical form.

The comparison of the contour plots in Figures 4 and 5 shows that $\overline{C}_d$ is lower for the ellipsoidal form than for the cylindrical form of tube cross section. For a given d_h, $\overline{C}_d$ decreases monotonically with $\overline{Re}$. If a value of $\overline{Re}$ is set, $\overline{C}_d$ has its
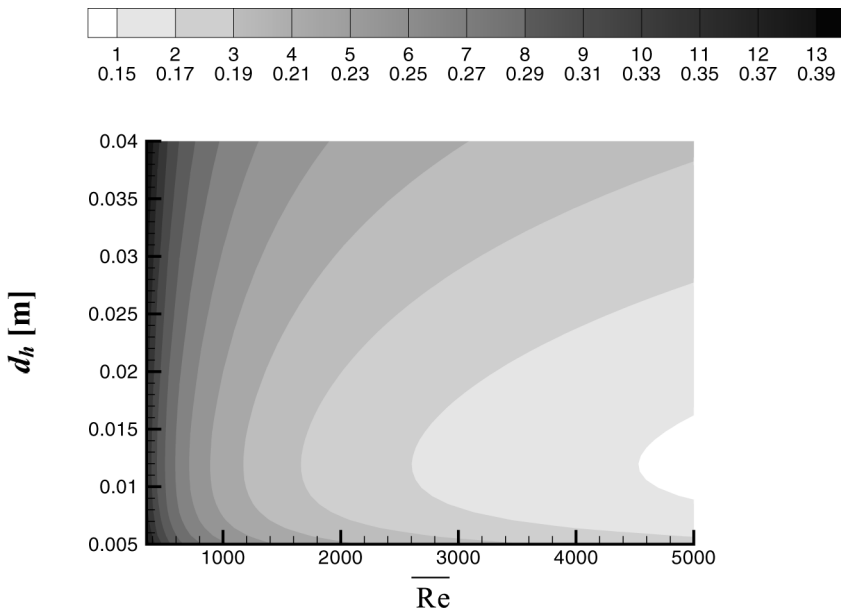

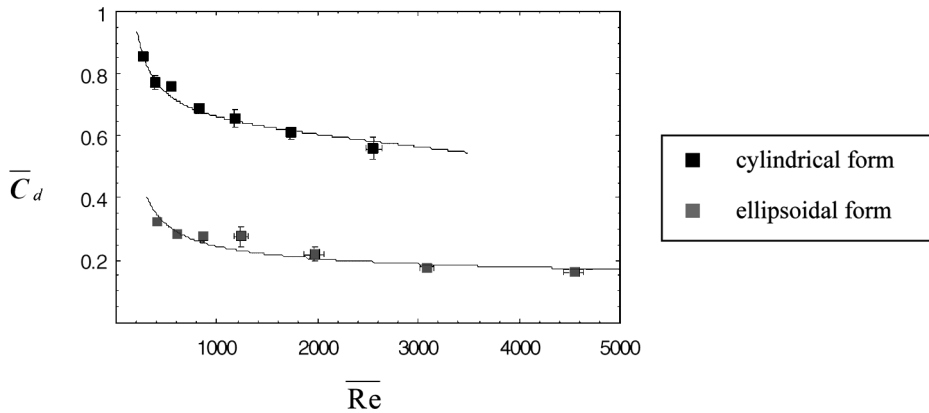**Figure 5.** Drag coefficient approximation function (15) for the ellipsoidal form.

Figure 6. Drag coefficient distribution for the cylindrical form ($d_h = 0.5824$ cm) and the ellipsoidal form ($d_h = 0.5649$ cm); $l/d = 1.125$.

minimum for a unique value of d_h. This value of hydraulic diameter, $d_h \approx 0.012$, is roughly the same for both forms.

In Figures 6–9, the drag coefficient functions (14) and (15) for $l/d = 1.125$, 1.25, 1.5, and 2.0 are compared with the discrete values of $\overline{C}_d$ (Table 3 and 4). The constructed polynomial functions (14) and (15) give a good approximation of the discrete values.

In the laminar region, at Reynolds numbers of a few hundreds, the flow reaches steady-state conditions. Furthermore, $\overline{C}_d$ decreases with increasing $\overline{Re}$ much more quickly than in the turbulent region. The transition is usually marked with strong oscillations, where flow changes direction periodically and the streamwise motion of the fluid becomes important. As a consequence, $\overline{C}_d$ increases sharply. Sharp increase of $\overline{C}_d$ (Figures 6–9) indicates that the transition
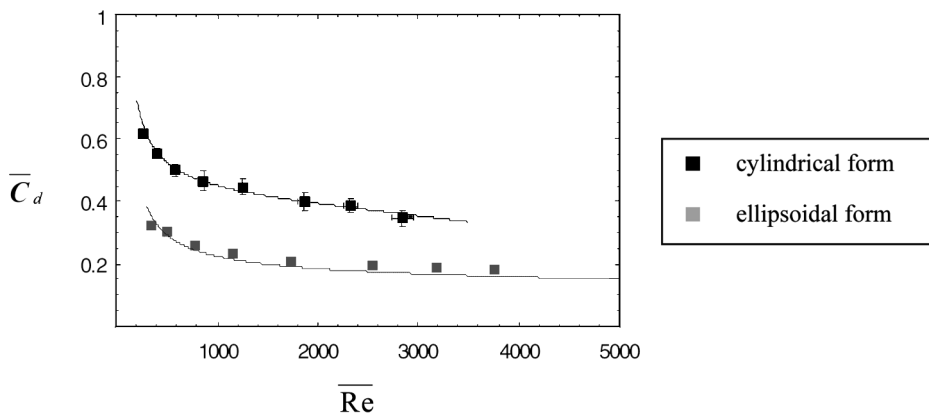
Figure 7. Drag coefficient distribution for the cylindrical form ($d_h = 0.9424$ cm) and the ellipsoidal form ($d_h = 0.9142$ cm); $l/d = 1.25$.
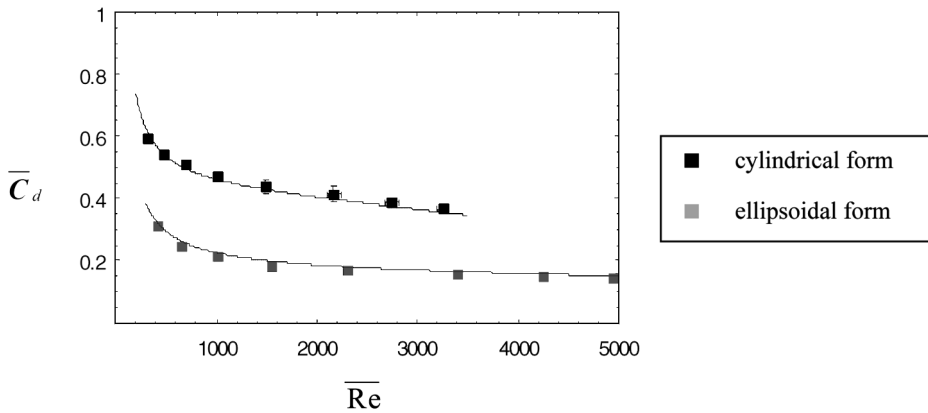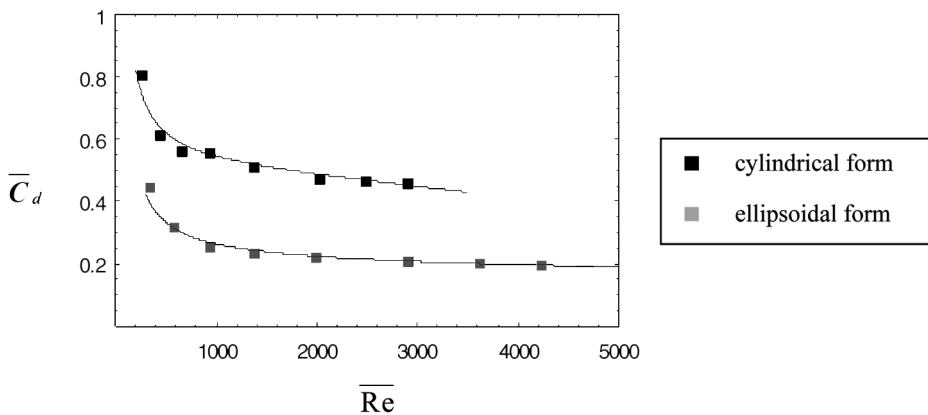
Figure 8. Drag coefficient distribution for the cylindrical form ($d_h = 1.776$ cm) and the ellipsoidal form ($d_h = 1.723$ cm); $l/d = 1.5$.

to turbulence occurs at slightly lower $\overline{Re}$ for the cylindrical form than for the ellipsoidal form of tube cross section. In the turbulent regime, $\overline{C}_d$ changes at a much slower rate, especially for the ellipsoidal form. Although the $\overline{C}_d$ for the cylindrical form is in general larger than the $\overline{C}_d$ for the elliptical form, the difference decreases with increasing d_h.

5.3. Stanton Number Functions

Using the recorded time distributions of Stanton number $St(t)$, the time-average $\overline{St}$ values were calculated for both forms of tube cross section and for the all imposed pressure drops (Table 2). The collected averages of $\overline{Re}$ and $\overline{St}$ are given in Table 5 for the cylindrical form and in Table 6 for the ellipsoidal form of tube cross section.

Figure 9. Drag coefficient distribution for the cylindrical form ($d_h = 3.899$ cm) and the ellipsoidal form ($d_h = 3.782$ cm); $l/d = 2.0$.

Table 5. Reynolds number $\overline{Re}$ and Stanton number $\overline{St}$ for the cylindrical form

l/d		1	2	3	4	5	6	7	8
1.125	$\overline{Re}$	258	385	549	816	1,178	1,733	2,557	—
	$\overline{St}$	0.094	0.073	0.061	0.049	0.042	0.035	0.031	—
1.25	$\overline{Re}$	266	397	590	865	1,248	1,870	2,328	2,841
	$\overline{St}$	0.094	0.074	0.059	0.049	0.041	0.034	0.029	0.026
1.5	$\overline{Re}$	321	473	692	1,019	1,489	2,169	2,746	3,258
	$\overline{St}$	0.097	0.074	0.060	0.048	0.040	0.034	0.030	0.028
2.0	$\overline{Re}$	274	443	655	935	1,373	2,029	2,497	2,909
	$\overline{St}$	0.132	0.097	0.078	0.064	0.052	0.044	0.039	0.038

Using the calculated averages (Tables 5 and 6), the Stanton number approximation functions were also determined with the least-squares method. These are polynomial functions of Reynolds number $\overline{Re}$ and hydraulic diameter d_h. For the cylindrical tube cross section, the function

$$\overline{St}(d_h, \overline{Re}) = -0.02388 + 6.774 \cdot 10^{-12} d_h^{-4} - 0.01714 d_h^{1/2}$$
$$+ 6.553\sqrt{d_h/\overline{Re}} + 2.090 \cdot 10^{-7} \overline{Re}^{-3} + 1.271 \overline{Re}^{-1/2}$$
$$+ 7.999 \cdot 10^{-6} \overline{Re} - 2.945 \cdot 10^{-13} \overline{Re}^3 \tag{16}$$

was obtained, whereas for the ellipsoidal tube cross section the following function was calculated:

$$\overline{St}(d_h, \overline{Re}) = 0.03716 + 1.529 \cdot 10^{-10} d_h^{-3} - 5.155 \cdot 10^{-5} d_h^{-1} + 0.02325\, d_h^{1/2}$$
$$+ 105.9\sqrt{d_h}/\overline{Re} + 0.7523 \overline{Re}^{-1} + 2.804 \cdot 10^{-4} \overline{Re}^{1/2} \tag{17}$$

Figures 10 and 11 present contour plots of the Stanton number polynomials for the cylindrical form (16) and for the ellipsoidal form (17) of tube cross section.

For the range of $\overline{Re}$ under consideration, the amount of heat transfer depends crucially on the momentum transfer from the fluid flow to the structure walls. Therefore, the $\overline{St}$ functions (Figures 10 and 11) are similar to the $\overline{C}_d$ functions (Figures 4 and 5). Stanton number decreases monotonically with increasing $\overline{Re}$ for any given d_h. This means that the flow velocity increases more quickly than the heat transfer from

Table 6. Reynolds number $\overline{Re}$ and Stanton number $\overline{St}$ for the ellipsoidal form

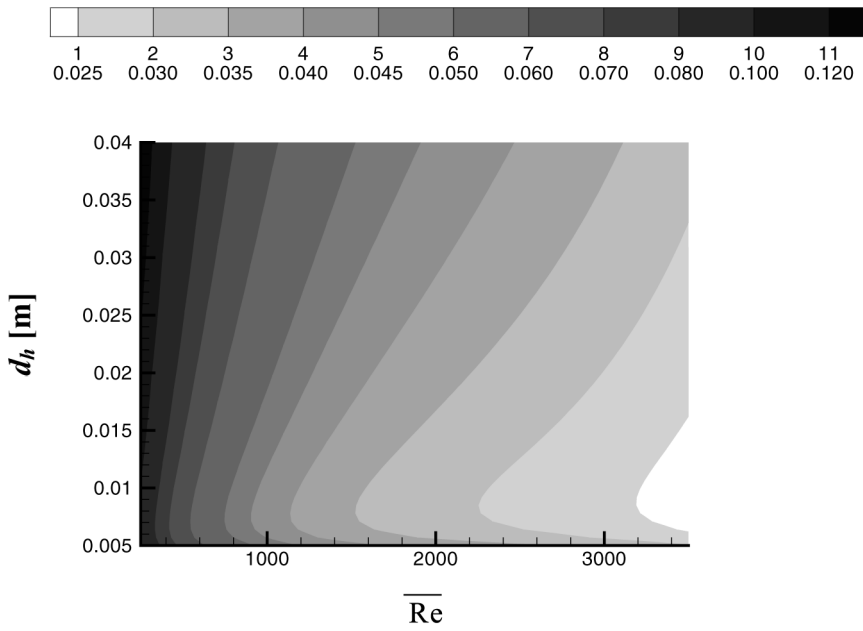| l/d		1	2	3	4	5	6	7	8
1.125	$\overline{Re}$	403	604	871	1,233	1,963	3,081	4,543	—
	$\overline{St}$	0.0437	0.038	0.033	0.030	0.023	0.018	0.016	—
1.25	$\overline{Re}$	351	513	783	1,167	1,743	2,550	3,179	3,753
	$\overline{St}$	0.061	0.051	0.039	0.032	0.027	0.024	0.022	0.020
1.5	$\overline{Re}$	422	670	1,025	1,553	2,312	3,396	4,255	4,957
	$\overline{St}$	0.070	0.052	0.041	0.034	0.028	0.025	0.023	0.021
2.0	$\overline{Re}$	351	590	934	1,381	1,999	2,915	3,626	4,234
	$\overline{St}$	0.091	0.075	0.056	0.046	0.038	0.032	0.029	0.027

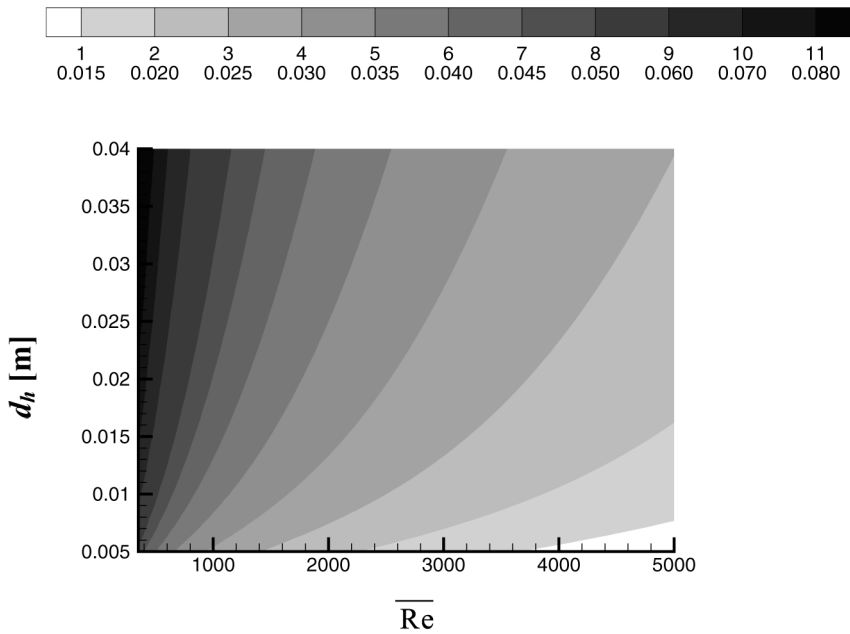**Figure 10.** Stanton number approximation function (16) for the cylindrical form.

Figure 11. Stanton number approximation function (17) for the ellipsoidal form.
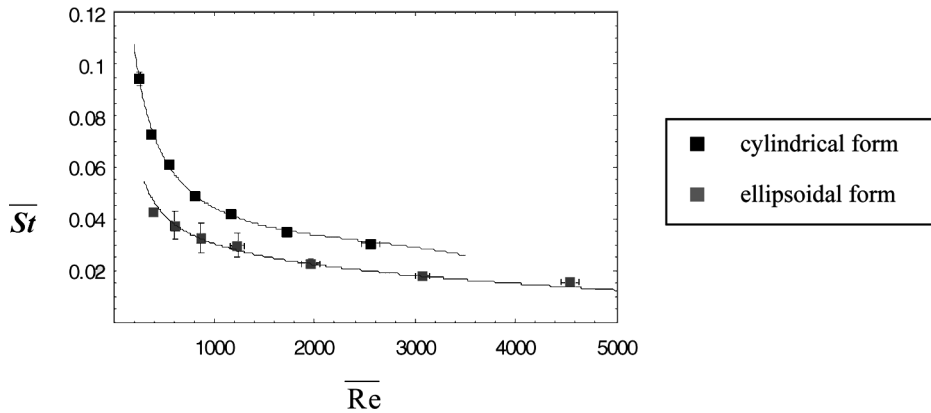
Figure 12. Stanton number distribution for the cylindrical form ($d_h = 0.5824$ cm) and the ellipsoidal form ($d_h = 0.5649$ cm); $l/d = 1.125$.

the isothermal walls to the fluid. Therefore, the temperature $T_f(t)$ as defined by (10) is actually decreasing with increasing $\overline{Re}$.

The contour plots (Figures 10 and 11) show that if $\overline{Re}$ is set, $\overline{St}$ drops rapidly at small values of d_h and then increases gradually with rising values of d_h. A comparison of the $\overline{C}_d$ and $\overline{St}$ functions shows that the minimum of $\overline{St}$ is located at a smaller d_h than the minimum of $\overline{C}_d$. This indicates decoupling of momentum and heat transfer between the flow and the structure, which was also observed and documented by other researches (e.g., [21]).

In Figures 12–15, the Stanton number functions (16) and (17) for $l/d = 1.125$, 1.25, 1.5, and 2.0 are compared with the discrete values of $\overline{St}$ (Tables 5 and 6). Again, the constructed polynomial functions (16) and (17) give a satisfactory approximation of the discrete values.
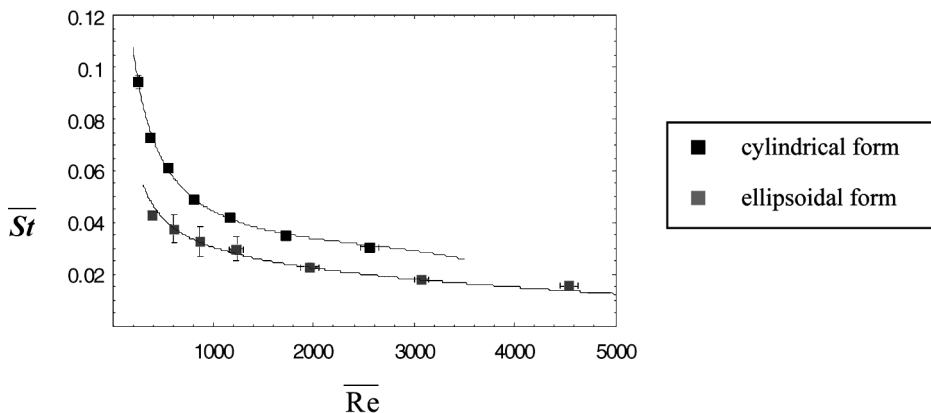

Figure 13. Stanton number distribution for the cylindrical form ($d_h = 0.9424$ cm) and the ellipsoidal form ($d_h = 0.9142$ cm); $l/d = 1.25$.
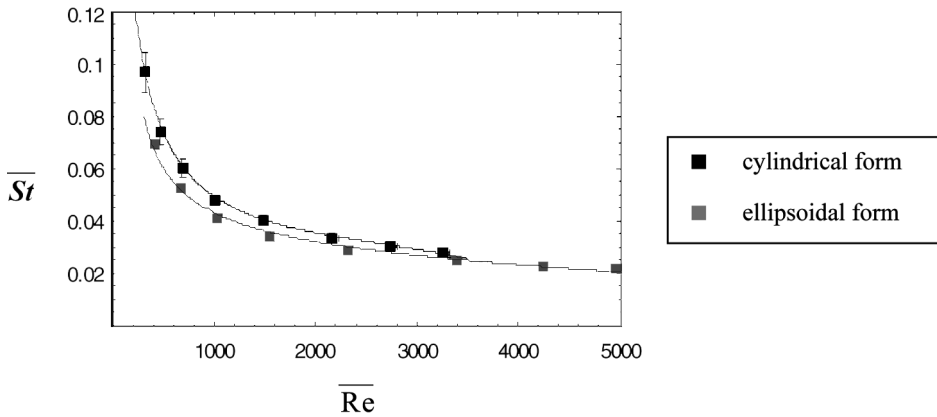
Figure 14. Stanton number distribution for the cylindrical form ($d_h = 1.776$ cm) and the ellipsoidal form ($d_h = 1.723$ cm); $l/d = 1.5$.
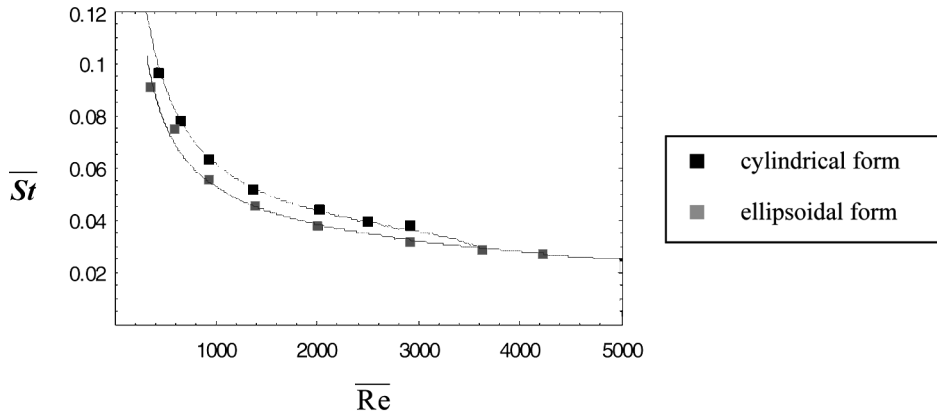

Figure 15. Stanton number distribution for the cylindrical form ($d_h = 3.899$ cm) and the ellipsoidal form ($d_h = 3.782$ cm); $l/d = 2.0$.

In the laminar region, $\overline{St}$ decreases more quickly with increasing $\overline{Re}$ than in the turbulent region. The transitional behavior that is evident from the calculated values of $\overline{C_d}$ (Figures 6–9) shows almost no influence on the $\overline{St}$ values.

Figures 12–15 show that $\overline{St}$ is larger for the cylindrical than for the ellipsoidal form of tube cross section. Although the difference is large for small d_h, it almost disappears at larger values of d_h.

6. CONCLUSIONS

Transient numerical simulations of heat transfer were performed for heat exchanger segments with cylindrical and ellipsoidal tubes in the staggered arrangement. Based on the calculated results, the time distributions of Reynolds number $Re(t)$, drag coefficient $C_d(t)$, and Stanton number $St(t)$ were obtained. It is

important to mention that we encounter much more complex physical behavior than is reported in the available literature (see [22–24]). Large flow oscillations and semi-stochastic motion of the flow in the spanwise direction were observed as the flow regime changes from laminar to turbulent.

The time-average values of Re(t), $C_d(t)$, and St(t) were used to construct the polynomial functions $\overline{C}_d(d_h, \overline{\text{Re}})$ and $\overline{\text{St}}(d_h, \overline{\text{Re}})$ for the cylindrical and elliptical tubes. These polynomial functions are to be used as input correlations for the integral model of a whole heat exchanger [16].

The calculated time-average values of $\overline{\text{Re}}$, $\overline{C}_d$, and $\overline{\text{St}}$ also enabled us to draw some conclusions on thermal effectiveness of the cylindrical and ellipsoidal forms of tube cross section. The drag coefficient $\overline{C}_d$ as well as the Stanton number $\overline{\text{St}}$ decrease monotonically with increasing $\overline{\text{Re}}$ for any hydraulic diameter d_h. On the other hand, $\overline{C}_d$ and $\overline{\text{St}}$ exhibit minima at a certain value of d_h for any given $\overline{\text{Re}}$. The value of d_h where $\overline{C}_d$ reaches its minimum is different from the value of d_h where the minimum of $\overline{\text{St}}$ is located.

In general, the values of $\overline{C}_d$ and $\overline{\text{St}}$ are lower for the ellipsoidal form in comparison to the cylindrical form of tube cross section. Although the differences are large for small d_h, they become smaller for larger values of d_h. This allows us to conclude that the influence of different forms of bounding surfaces diminishes with increasing d_h.

REFERENCES

 1. A. A. Zhukauskas, Convective Heat Transfer in Cross Flow, In S. Kakac, R. K. Shah, and W. Aung (eds.), *Handbook of Single-Phase Convective Heat Transfer*, Wiley, New York, 1987.
 2. W. S. Kays and A. L. London, *Compact Heat Exchangers*, 3rd ed., Krieger, Malabar, FL, 1998.
 3. S. Kakac, *Heat Exchangers: Thermo-Hydraulic Fundamentals and Design*, 2nd ed., Hemisphere, New York, 1985.
 4. S. Aiba, H. Tsuchida, and T. Ota, Heat Transfer around Tubes in In-line Tube Banks, *Bull. Jpn. Soc. Mech. Eng.*, vol. 25, no. 204, pp. 919–926, 1982.
 5. B. E. Launder and T. H. Massey, The Numerical Prediction of Viscous Flow and Heat Transfer in Tube Banks, *J. Heat Transfer*, vol. 100, pp. 565–571, 1978.
 6. K. A. Antonopoulos, Prediction of Flow and Heat Transfer in Rod Bundles, Ph.D. thesis, Mechanical Engineering Department, Imperial College, London, UK, 1979.
 7. C. H. Amon and B. B. Mikic, Spectral Element Simulations of Unsteady Forced Convective Heat Transfer. Application to Compact Heat Exchanger Geometries, *Numer. Heat Transfer A*, vol. 19, no. 1, pp. 1–19, 1991.
 8. D. Yu, R. F. Barron, T. A. Ameel, and R. O. Warrington, Mixed Convection from Horizontal Tube Banks between Two Vertical Parallel Plates, *Numer. Heat Transfer A*, vol. 27, no. 4, pp. 473–486, 1995.
 9. M. C. Sharatchandra, Turbulent Flow and Heat Transfer in Staggered Tube Banks with Displaced Tube Rows, *Numer. Heat Transfer A*, vol. 31, no. 6, pp. 611–627, 1997.
10. H. R. Barsamian and Y. A. Hassan, Large Eddy Simulation of Turbulent Crossflow in Tube Bundles, *Nuclear Eng. Design J.*, vol. 172, pp. 103–122, 1997.
11. M. Prithiviraj and M. J. Andrews, Three-Dimensional Numerical Simulation of Shell-and-Tube Heat Exchangers. Part 1: Foundation and Fluid Mechanics, *Numer. Heat Transfer A*, vol. 33, no. 8, pp. 799–819, 1998.

12. S. B. Beale and D. B. Spalding, A Numerical Study of Unsteady Fluid Flow in In-line and Staggered Tube Banks, *J. Fluids Struct.*, Vol. 13, pp. 723–754, 1999.
13. M. Tutar and A. Akkoca, Numerical Analysis of Fluid Flow and Heat Transfer Characteristics in Three-Dimensional Plate Fin-and-Tube Heat Exchangers, *Numer. Heat Transfer A*, vol. 46, no. 3, pp. 301–321, 2004.
14. A. Horvat and B. Mavko, Hierarchic Modeling of Heat Transfer Processes in Heat Exchangers, *Int. J. Heat Mass Transfer*, vol. 48, pp. 361–371, 2005.
15. S. V. Patankar and D. B. Spalding, A Calculation Procedure for the Transient and Steady-State Behaviour of Shell-and-Tube Heat Exchangers, Imperial College of Science and Technology, London, UK, 1972.
16. A. Horvat and I. Catton, Numerical Technique for Modeling Conjugate Heat Transfer in an Electronic Device Heat Sink, *Int. J. Heat Mass Transfer*, vol. 46, pp. 2155–2168, 2003.
17. R. B. Bird, W. E. Stewart, and E. N. Lightfoot, *Transport Phenomena*, Wiley, New York, 1960.
18. F. R. Menter, Zonal Two-Equation k–ω Turbulence Models for Aerodynamic Flows, AIAA Paper 93–2906, 1993.
19. D. C. Wilcox, Multiscale Model for Turbulent Flows, *Proc. AIAA 24th Aerospace Sciences Meeting*, American Institute of Aeronautics and Astronautics, 1986, p. 37.
20. F. R. Menter, Two-Equation Eddy-Viscosity Turbulence Models for Engineering Applications, *AIAA J.*, vol. 32, no. 8, pp. 37–40, 1994.
21. K. Inaoka, J. Yamamoto, and K. Suzuki, Dissimilarity between Heat Transfer and Momentum Transfer in a Disturbed Turbulent Boundary Layer with Insertion of a Rod—Modeling and Numerical Simulation, *Int. J. Heat Fluid Flow*, vol. 20, no. 3, pp. 290–301, 1999.
22. A. Bejan, *Convection Heat Transfer*, 2nd ed., Wiley, New York, 1995.
23. G. Stanescu, A. J. Fowler, and A. Bejan, The Optimal Spacing of Cylinders in Free-Stream Cross-Flow Forced Convection, *Int. J. Heat Fluid Flow*, vol. 39, no. 2, pp. 311–317, 1996.
24. R. S. Matos, J. V. C. Vergas, T. A. Laursen, and A. Bejan, Optimally Staggered Finned Circular and Elliptic Tubes in Forced Convection, *Int. J. Heat Fluid Flow*, vol. 47, pp. 1347–1359, 2004.

APPENDIX

Table 7. Number of grid nodes used in REV with the cylindrical tube cross section

l/d	1	2	3	4	5	6	7	8
1.125	54,811	54,811	89,428	89,428	114,500	173,550	350,245	—
1.25	71,445	71,445	71,445	158,669	158,669	222,296	222,296	222,296
1.5	89,525	89,525	89,525	89,525	180,002	180,002	180,002	180,002
2.0	79,047	79,047	79,047	79,047	79,047	79,047	116,734	116,734

Table 8. Number of grid nodes used in REV with the ellipsoidal tube cross section

l/d	1	2	3	4	5	6	7	8
1.125	57,834	57,834	57,834	180,618	180,618	180,618	213,225	—
1.25	87,097	87,097	87,097	87,097	137,600	205,476	205,476	205,476
1.5	119,309	119,309	119,309	119,309	119,309	174,752	174,752	174,752
2.0	95,641	95,641	95,641	95,641	95,641	186,868	186,868	186,868